Computers & Fluids 86 (2013) 14–27

Contents lists available at ScienceDirect

Computers & Fluids

journal homepage: www.elsevier.com/locate/compfluid

The direction decoupled Quiet Direct Simulation method for rapid simulation of axisymmetric inviscid unsteady flow in pulsed pressure chemical vapour deposition

C.W. Lim [a,b], M.R. Smith [c], H.M. Cave [a,d], M.C. Jermy [a,*], J.-S. Wu [d], S.P. Krumdieck [a]

[a] Department of Mechanical Engineering, University of Canterbury, Private Bag 4800, Christchurch 8140, New Zealand
[b] Department of Mechanical Engineering, University of Tenaga Nasional, Jalan IKRAM-UNITEN, 43000 Kajang, Selangor, Malaysia
[c] National Center for High Performance Computing, National Applied Research Laboratories, No. 7 R&D Road VI, Hsinchu Science Park, Hsinchu 30050, Taiwan
[d] Department of Mechanical Engineering, National Chiao-Tung University, 1001 Ta-Hsueh Road, Hsinchu 30050, Taiwan

ARTICLE INFO

Article history:
Received 31 October 2011
Received in revised form 10 January 2013
Accepted 10 July 2013
Available online 17 July 2013

Keywords:
QDS
Gas kinetic solver
Shock-bubble interaction
Forward-facing cylinder
Numerical dissipation
PP–CVD

ABSTRACT

Pulsed Pressure–Chemical Vapour Deposition (PP–CVD) is a thin film deposition process which employs a highly unsteady flow with wide dynamic range of pressure. The large, time-varying density gradient during a PP–CVD process cycle produces a flow field in which the Knudsen number varies from the near-continuum to the rarefied regimes, making Direct Simulation Monte Carlo (DSMC) prohibitively expensive. The present directional decoupled Quiet Direct Simulation (DD-QDS) method is a novel kinetic-based flux scheme that computes fluxes of mass, momentum and energy at the interface of computational cells in a highly computationally efficient manner. The Maxwell–Boltzmann equilibrium distribution is enforced locally at each computational cell at each time step. In this paper, an axisymmetric second order directional decoupled QDS scheme is used to simulate highly unsteady flows encountered in PP–CVD reactor. Two simulations were conducted to investigate the PP–CVD reactor flow field at 1 Pa and 1 kPa reactor base pressures. The assumption of the local Maxwell–Boltzmann equilibrium distribution used in the QDS scheme is verified by examining the gradient length local Knudsen number based on the density, and by estimating the average number of molecular collisions within each computational cell in one computational time step. The validity of the local equilibrium assumption is found satisfactory at 1 kPa reactor based pressure but not at 1 Pa. The limitation of the QDS scheme in modelling PP–CVD flow was also investigated. The time required to establish the quasi-steady under-expanded jet is found to be ~4 ms, and the jet dissipates within 0.5 ms of the end of injection. This important information is required to set up PP–CVD operating conditions which give uniform film deposition.

1. Introduction

1.1. Development of the direction decoupled Quiet Direct Simulation method

There are a number of approaches for the simulation of gas flows and a large variety of solution methods depending on the nature and level of rarefaction of the flow. In the conventional Computational Fluid Dynamics (CFD) approach, finite volume methods have been used extensively to solve the Euler or Navier–Stokes equations. Due to the complexity of the governing equations, computational cost is high in the conventional CFD methods particularly if a turbulence model, for which extra equations must be solved, is required in the simulation. There is also usually the need of extra care in meshing of the computational domain in order to ensure accurate results, convergence and stability of the simulation. In addition, in unsteady flow simulation, it would be difficult to generate a fixed computational mesh suitable for the constantly changing flow field. An adaptive mesh may be used in order to ensure the grid alignment with the flow but this requires extra computational resources which may reduce the computational efficiency.

An alternative is a kinetic-theory based approach that takes into account the particle-based nature of gases in simulating the flow field. The most widely-accepted particle-based direct simulation method is the Direct Simulation Monte Carlo (DSMC) technique developed in the 1960s by Bird [1]. The DSMC algorithm requires the use of random numbers and is thus subject to statistical scatter and requires averaging over a large number of time steps to reduce the scatter in the sampled macroscopic properties. Another particle-based kinetic-theory approach is Pullin's Equilibrium Particle Simulation Method (EPSM) [2]. EPSM simplified the collision phase

* Corresponding author. Tel.: +64 (3)364 2987x7390; fax: +64 (3)364 2078.
E-mail address: mark.jermy@canterbury.ac.nz (M.C. Jermy).

0045-7930/$ - see front matter © 2013 Elsevier Ltd. All rights reserved.
http://dx.doi.org/10.1016/j.compfluid.2013.07.012

computation in DSMC in which simulated particles are assigned new velocities from the local Maxwell–Boltzmann velocity distribution. However, since the velocities are drawn randomly from the distribution, EPSM also exhibits statistical scatter in the results and as such requires averaging over a large number of time steps in the same way as DSMC.

Another kinetic theory-based approach is the flux-based simulation method. An example of the flux-based kinetic-theory approach is Pullin's Equilibrium Flux Method (EFM) [2]. This method employs split fluxes which are calculated across the interface of two cells by taking the moments of the equilibrium velocity probability function at the interface location. The technique is not subject to the statistical scatter inherent in particle-based methods, however, it involves the use of error function extensively which is computationally complex and expensive to evaluate.

The Quiet Direct Simulation (QDS) method was originally termed Quiet Direct Simulation Monte Carlo (QDSMC) when developed by Albright et al. as a method for modelling plasmas [3] and Eulerian fluids [4]. Smith et al. [5] then reformulated QDSMC to be a conservative finite volume scheme and implemented to second order accuracy. The reformulated QDSMC scheme was renamed QDS due to the lack of stochastic processes. The QDS method is a flux-based kinetic-theory approach which the continuous distribution function employed in previous kinetic-theory based methods is replaced by a discrete mass probability distribution function. The QDS method assumes a sufficiently high collision rate in each computational cell such that the velocity distribution relaxes completely to the Maxwell–Boltzmann local equilibrium distribution during the time step. A Gaussian quadrature (or Gauss–Hermite quadrature) is used to approximate the Maxwell–Boltzmann equilibrium condition. It has been shown that the application of Gauss–Hermite quadrature to the computation of the discrete mass probability distribution function requires only a low number ($\leqslant 4$ in general) of discrete velocities to obtain results virtually indistinguishable from the equivalent continuum results obtained from EFM [5].

The QDS method described in [5] is advantageous for its simplicity, its computational efficiency requiring no evaluation of computationally expensive functions, its deterministic approach eliminating statistical scatter inherent in the DSMC solvers, its localised computation with only the nearest neighbour information required for second order spatial accuracy allowing easy implementation for parallel computation, it is easily extended to multiple spatial dimensions and multiple gas species, and it is unconditionally stable. Yet, it is numerically diffusive and due to the assumption of perfect local equilibrium is capable of solving only inviscid flows at present.

For application to cylindrical or spherically axisymmetric flows, the traditional implementation of QDS would require consideration of volumetric effects on the flux computation. This can become involved when (i) extended to multiple dimensions, or (ii) fluxes are extended to higher order spatial accuracy. Hence, in this paper, the basic QDS scheme [5] is recast as an approximation to the EFM to extend its application to axisymmetric flows, in a manner familiar in conventional CFD, and named as directional decoupled QDS (DD-QDS). It is tested against standard test cases and applied the simulation of the unsteady complex flow encountered in Pulsed Pressure Chemical Vapour Deposition (PP–CVD) process.

1.2. Pulsed pressure chemical vapour deposition process

PP–CVD is a novel manufacturing technique developed by Versteeg et al. [6] to deposit thin films of solid material onto a substrate through a chemical process in repeated pulses. It has shown improved performance over conventional Chemical Vapour Deposition (CVD) methods including high precursor conversion efficiency, film quality and substrate conformity [7–9]. The operating cycle of the PP–CVD process consists of an injection and pump-down phase. During the injection phase, a controlled volume of precursor solution at high supply pressure is injected into a continuously evacuated reactor volume via an ultrasonic atomizer or choked orifice. The injection of precursor mixture is carried out rapidly in the partially evacuated reactor volume, increasing reactor pressure to a maximum. The process is followed by a pump-down phase when the reactor inlet valve is closed while the reactor volume is continuously evacuated by a vacuum pump to achieve a set minimum pressure before the next pulse cycle begins. The rapid injection of precursor solution leads to a high vapour concentration near the reactor inlet during the injection phase while the continuously evacuated reactor chamber causes the fluid density to reduce significantly with time after the end of the injection phase, and with the distance from the inlet. This pulsed process cycle causes a highly unsteady flow field with large density gradients throughout the reactor volume.

Previous numerical modelling of the PP–CVD flow field by Cave [10] using the unsteady DSMC modelling technique developed by Bird [11] found that the highly unsteady nature of the flow makes DSMC simulations extremely computationally expensive. The unsteady flow phenomena coupled with significant density gradient over the flow field also challenges conventional Navier–Stokes CFD solvers. Obtaining converged solutions at an acceptable computational expense using either DSMC or conventional Navier–Stokes solver is particularly difficult for such unsteady flow fields. For these reasons, in this paper, QDS has been investigated as a candidate method for rapid approximation of the PP–CVD flow field with acceptable accuracy. A speedy solution is essential particularly in the customisation of the PP–CVD reactor design and operational conditions selection in meeting a specific application of the thin film deposition technique. The limitations, arising from the assumption of local thermal eqauilibrium, on the accuracy of the QDS solution are explored.

2. Method

The Maxwell–Boltzmann equilibrium velocity distribution function has the form of:

$$p(v) = \frac{1}{\sqrt{2\pi}\sigma} \exp\left(\frac{-(v-u)^2}{2\sigma^2}\right) \tag{2.1}$$

where $p(v)dv$ is the probability of finding a molecule with a velocity in the range $v \rightarrow v + dv$, u is the bulk velocity and the velocity variance $\sigma = \sqrt{RT}$. The integration of moments of Eq. (2.1) over infinite velocity range can be represented by introducing the Heaviside step function H_s. This permits the fluxes splitting to approximate the EFM flux expressions given in Eq. (2.2) as:

$$\int_{-\infty}^{\infty} \frac{e^{-(v-u)^2/2\sigma^2}}{\sqrt{2\pi}\sigma} f(v)dv \approx \sum_{j=1}^{N} H_s(-q_j) w_j f(q_j) + \sum_{j=1}^{N} H_s(q_j) w_j f(q_j) \tag{2.2}$$

where $f(v)$ takes the value 1 if the mass flux is to be computed, the value v if the momentum flux is computed, and v^2 if the energy flux is computed. $H_s(x) = 1$ if $x > 0$, else $H_s(x) = 0$ while w_j and q_j are the weights and abscissas of the Gauss–Hermite parameters. The abscissas are the roots of the Hermite polynomials which can be defined by:

$$H_{n+1}(q) = 2qH_n - 2nH_{n-1} \tag{2.3}$$

where $H_{-1} = 0$ and $H_0 = 1$. The weights can be determined from:

$$w_j = \frac{2^{n-1} n! \sqrt{\pi}}{n^2 [H_{n-1}(q_i)]^2} \tag{2.4}$$

The Gauss–Hermite parameters are tabulated by Zwillinger [12]. Eq. (2.2) becomes exact when the function $f(v)$ is a linear combination of the $2N-1$ polynomials $x^0, x^1, \ldots, x^{2N-1}$. Therefore, in the QDS method, the Maxwell–Boltzmann equilibrium velocity distribution function can be discretized with a chosen number of N "velocity bins" in each spatial dimension ($N \leqslant 4$ in general) where the mass fraction of the computational cell carried in each bin is determined by the weights of the Gauss–Hermite quadrature while the associated velocities are represented by the corresponding abscissas.

Consider a typical one dimensional cell surface with the conserved macroscopic properties η given as:

$$\eta = \begin{bmatrix} \rho \\ \rho u \\ \rho\left(\frac{1}{2}u^2 + c_p T\right) \end{bmatrix} \tag{2.5}$$

where ρ is the density, c_p is the specific heat for constant pressure. By using the velocity distribution function and the conserved properties on either side of the surface, the net flux of η, F_η, across the cell surface can be expressed as:

$$F_\eta = F_\eta^+ + F_\eta^- \tag{2.6}$$

where the superscripts + and − denote conditions on the left and right of the surface, respectively. The flux due to the gas molecules transporting from the left to the right of the surface can be determined by evaluating the integral given as:

$$F_\eta^+ = \int_0^\infty v\eta^+ f(v) dv \tag{2.7}$$

while the flux due to the gas molecules transporting from the right to the left of the surface is computed by evaluating the integral given as:

$$F_\eta^- = \int_{-\infty}^0 v\eta^- f(v) dv \tag{2.8}$$

Using the equilibrium molecular velocity distribution on either side of the surface, Eq. (2.7) can then be evaluated by Eq. (2.9) by letting the thermal velocity $v' = v - u$ and taking the moments of the conserved macroscopic property η around $f(v')$ as:

$$F_{\eta,QDS}^+ = \int_0^\infty (v' + u)\eta^+ f(v') dv' \approx \sum_{j=1}^N H_S(v_j) v_j w_j \eta_j^+ \tag{2.9}$$

Similarly, Eq. (2.8) can be evaluated by Eq. (2.10) as:

$$F_{\eta,QDS}^- = \int_{-\infty}^0 (v' + u)\eta^- f(v') dv' \approx \sum_{j=1}^N H_S(-v_j) v_j w_j \eta_j^- \tag{2.10}$$

where η_j are the conserved macroscopic properties of the jth QDS "velocity bin" given as:

$$\eta_j = \begin{bmatrix} \rho \\ \rho v_j \\ \rho\left(\frac{1}{2}v_j^2 + \varepsilon_j\right) \end{bmatrix} \tag{2.11}$$

where $v_j = v_j = u + \sqrt{2\sigma^2} q_j$ velocity of the bin and ε_j is the internal energy of molecular structure in the bin such as rotational, vibrational, or electronic energy.

Consider a control volume element of the flow field for a computational cell as shown in Fig. 1, the conserved macroscopic properties of cell i updated after one time step $k+1$ can be computed by applying the divergence theorem and given as:

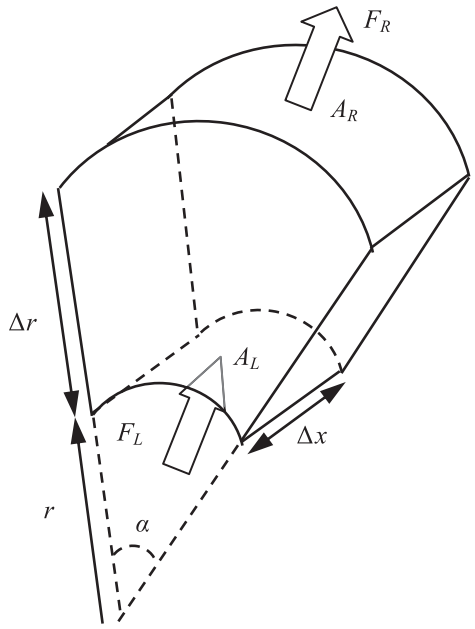

Fig. 1. Control volume element for a single cell of a cylindrically axisymmetric geometry.

$$\eta_i^{k+1} = \eta_i^k - \frac{\Delta t}{V}\left(F_R A_R - F_L A_L + \eta_{i,P}^k\right) \tag{2.12}$$

where V is the cell volume, F is the net flux normal to the surface of area A and subscripts R and L indicate reference to conditions on the left and right sides of the cell interface (or top and bottom sides of an annular cylindrical cell as shown in Fig. 1), respectively. $\eta_{i,p}$ is the momentum correction applied to account the pressure change along control volume elements in the radial direction for axisymmetric flows given as:

$$\eta_{i,P} = \begin{bmatrix} 0 \\ P_i \alpha \Delta r \\ 0 \end{bmatrix} \tag{2.13}$$

where P_i is the cell pressure, Δr is the cell width in the radial direction and α is the axisymmetric angle (usually π).

In the second order scheme, the split fluxes at the cell interface are reconstructed in a manner similar to the conventional reconstruction method [13]. Hence, by taking a Taylor series expansion of the split fluxes at the cell interface, a second order accurate expression for the net fluxes F_R and F_L are given in Eqs. (2.14) and (2.15), respectively, as:

$$F_R = F_{i+\frac{1}{2}}^+ + F_{i+\frac{1}{2}}^- = \left[F_i^+ + \frac{\Delta r}{2}\left(\frac{dF^+}{dr}\right)_i\right] + \left[F_{i+1}^- - \frac{\Delta r}{2}\left(\frac{dF^-}{dr}\right)_{i+1}\right] \tag{2.14}$$

$$F_L = F_{i-\frac{1}{2}}^- + F_{i-\frac{1}{2}}^+ = \left[F_i^- + \frac{\Delta r}{2}\left(\frac{dF^-}{dr}\right)_i\right] + \left[F_{i+1}^+ - \frac{\Delta r}{2}\left(\frac{dF^+}{dr}\right)_{i-1}\right] \tag{2.15}$$

where the flux gradients dF/dr are calculated from the finite difference approximations of F^+ and F^- using a slope limiter to maintain positivity. The gradients of the fluxes are determined using the MINMOD (Minimum Modulus) or the MC (Monotonized Central Difference) slope limiter [14]. For example, the gradient in radial flux calculation using the MC slope limiter is given as:

$$\left(\frac{dF^+}{dr}\right)_i = \text{MINMOD}\left[\frac{F_{i+1}^+ - F_{i-1}^+}{2\Delta r},\ \text{MINMOD}\left(2\frac{F_{i+1}^+ - F_i^+}{\Delta r}, 2\frac{F_i^+ - F_{i-1}^+}{\Delta r}\right)\right] \tag{2.16}$$

where the MINMOD slope limiter [15] is given as:

$$\text{MINMOD}[a,b] = \begin{cases} 0 & \text{if SIGN}(ab) < 0 \\ a & \text{if SIGN}(ab) > 0 \text{ and } |a| < |b| \\ b & \text{if SIGN}(ab) > 0 \text{ and } |b| < |a| \end{cases} \quad (2.17)$$

A variable time step scheme is used to maintain the maximum kinetic Courant–Friedrichs–Levy (CFL) number in the domain below a desired value (usually $\leqslant 1$). Unlike the implementation in [5], the present implementation is not unconditionally stable, so the CFL number is limited to maintain both stability and physical realism. For a two-dimensional or axisymmetric simulation, the CFL number is given by:

$$\text{CFL} = \max\left[\frac{\left(u_x + q_{j(\max)}\sqrt{RT_i}\right)\Delta t}{\Delta x}, \frac{\left(u_r + q_{j(\max)}\sqrt{RT_i}\right)\Delta t}{\Delta r}\right] \quad (2.18)$$

where $q_{j(\max)}$ is the maximum value of the velocity bin abscissas (i.e. the value which gives the maximum thermal velocity).

In the current implementation boundary conditions are handled using ghost cells [5]. These cells can be used to represent walls, stream boundaries, inflow boundaries and zero-gradient outflow boundaries. The interaction of a gas with a wall is identical to the interaction of that flow with an adjacent cell having the same flow properties but a reversed flow direction normal to the wall. This enforces the no-slip condition at the wall itself. For the inflow boundaries, the ghost cells have properties equal to the free stream conditions, whereas the conditions in outflow ghost cells are extrapolated from values within the adjacent flow field cells. In both cases, fluxes from flow field cells to inflow/outflow ghost cells are destroyed.

3. Validation cases

3.1. 1D spherically imploding shock wave

A one-dimensional simulation of a spherically imploding shock wave has been used to verify the accuracy of the axisymmetric implementation of QDS. Following the investigations by Ponchaut et al. [16], a shock wave (Mach no. of 5) travelling towards the centre is positioned at a radial location of r at $t = 0$. This problem is introduced and discussed briefly here, and details can be found in [16]. Conditions at a radial distance of $0.1r$ as a function of time t were employed to validate the numerical solutions. Solutions generated with the DD-QDS algorithm are shown in Fig. 2.

The DD-QDS simulation was conducted with 800 cells and a second-order spatial accuracy using a MINMOD limiter to ensure positivity. Since the gas is ideal ($\gamma = 1.4$) and inviscid, this problem has no characteristic length [16]. Hence, the variables ρ, u and time t shown in Fig. 2 are normalised by the undisturbed density in region I (ρ_I), u_{ref} and t_{ref}, respectively, where u_{ref} and t_{ref} are the velocity and time at which the imploding shock passes the location at $0.1r$. The regions I (undisturbed gas, prior to the arrival of the incoming shock), II (post incoming shock, pre-shock reflection), III (post shock reflection, pre-reflected shock) and IV (post reflected shock) are clearly shown and in good agreement with numerical and theoretical solutions provided by Ponchaut et al. [16].

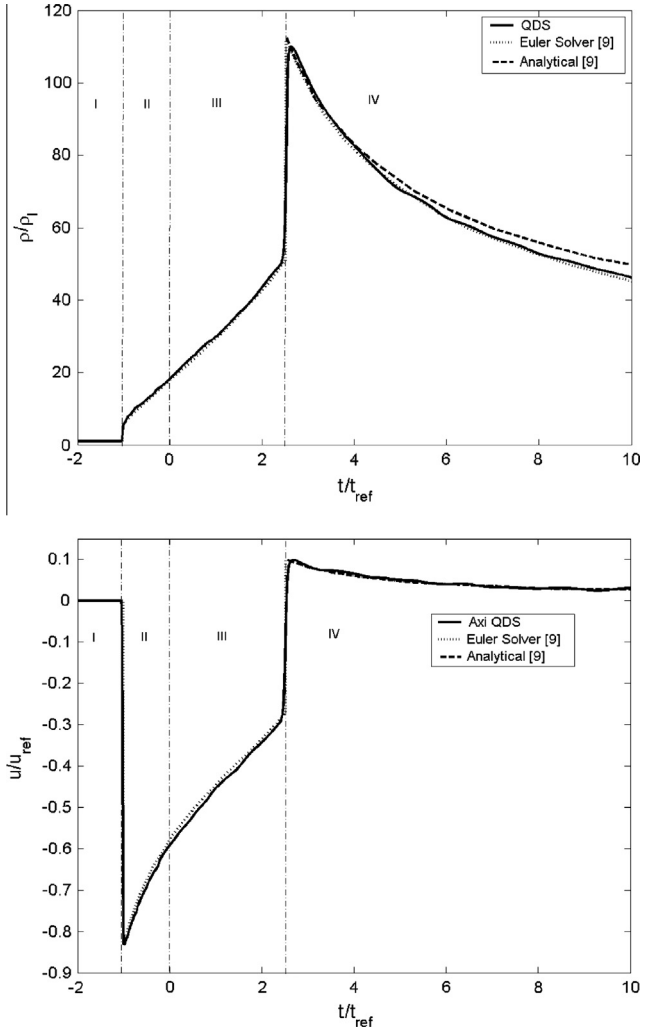

Fig. 2. Normalised density (top) and velocity (bottom) profiles taken from radial location $0.1r$ (where r is the initial shock location) for a spherically imploding shock ($M_S = 5.0$). The QDS solution (using three sample points, or velocity bins, per pair of split fluxes) employs 800 cells with second order spatial accuracy using a MINMOD limiter. Results are compared with numerical and analytical solutions from Ponchaut et al. [16]. The gas is assumed ideal ($\gamma = 7/5$) and inviscid.

3.2. Shock-bubble interaction

As a validation of the accuracy of the DD-QDS code, a test problem for the interaction of shock waves with a spherical bubble was simulated. The problem of shock-bubble interaction was first studied experimentally by Rudinger and Somers to understand the fundamental mechanics associated with turbulence generation and mixing [17]. Haas and Sturtevant then studied this problem to investigate the nature of shock refraction at low Mach number [18]. Numerical simulations on this problem have also been carried out to study the Mach number effects on the shock-bubble interaction [19]. Most of these simulations involve multi-species flow. As the present DD-QDS code simulates single species flow, the results are compared to a simulation using the EFM method. Fig. 3 shows the geometry of the problem together with the initial and boundary conditions for the simulation of shock-bubble interaction in a 1.0 unit length cylindrical channel with radius of 0.5 unit length. The spherical bubble with radius $r = 0.2$ unit length is initially located at 0.4 unit length downstream from the channel inlet. The simulated gas was ideal gas with a ratio of specific heats of 1.4 and a gas constant of $R = 1.0$. The inlet boundary was kept at the initial flow condition at all times while the outflow condition was extrapolated from the adjacent flow field cells. Reflecting wall boundary conditions were applied along the walls of the tunnel.

The simulation was conducted with the axisymmetric DD-QDS code by using 3 velocity bins per coordinate direction and the MINMOD slope limiter in calculating property gradients. In the simulation, 200 radial cells and 400 axial cells are used. The computational cells of the bubble were generated at $t = 0$ in a staircase

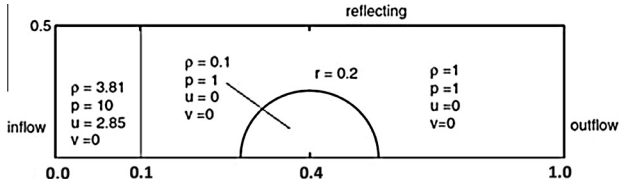

Fig. 3. Geometry, boundary and initial conditions for the simulation of shock-bubble interaction.

manner with the cells taking the properties of either the bubble or the surroundings, but never values in between. A dynamic time step was used in which the simulation time step was adjusted after each time step to maintain CFL < 0.25 everywhere. The simulation was carried out until 0.2 s when the shock wave is just about to reach the outflow boundary.

The DD-QDS simulation result was compared to that of the simulation using EFM [20] as validation. Fig. 4 shows the comparison of density contour between the simulation results of the DD-QDS solver and the EFM solver at the simulation time of 0.2 s. As a consequence of interaction of a right-moving incident shock, the bubble region with lower density than the surroundings expands radially outward and deforms into a kidney-shape vortex as a re-entrant jet forms at the upstream interface, as visualised by Haas and Sturtevant [18] and also predicted by Picone and Boris [19] and Bagabir and Drikakis [21]. The comparison shows that the DD-QDS solver is able to capture similar shock-bubble interaction flow field features similar to the EFM. The backward-moving reflected shock and right-moving transmitted shock have almost exact match in position to that in the EFM's result. This shows the DD-QDS scheme's capacity for producing close approximations to the problem with a simple formulation and high computational efficiency. Both simulations, using the DD-QDS and the EFM, were carried out on a single desktop computer with 3.00 GHz Intel Core 2 Duo CPU E6850 processor and 4 GB of RAM. The simulation consumed 254 s to compute 0.2 s flow using the DD-QDS solver compared to 369 s by using EFM solver. Hence, DD-QDS solver has significantly greater computational efficiency equivalent accuracy to EFM for this problem.

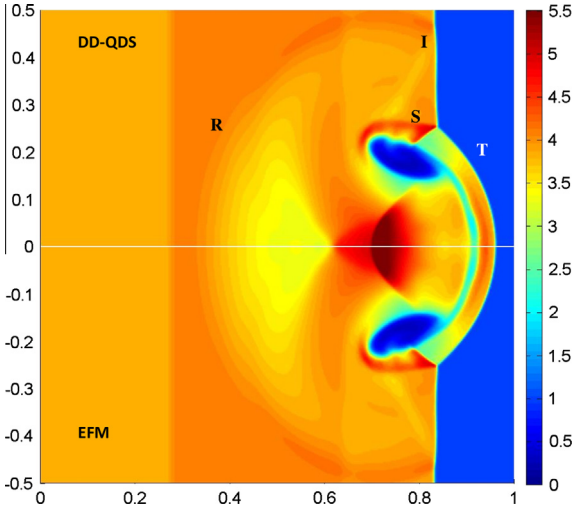

Fig. 4. Comparison of density contour at 0.2 s for shock-bubble interaction simulation between results from the present QDS scheme (top) and results from the EFM (bottom); *I* is the incident shock, *R* is the reflected shock, *T* is the transmitted shock, and *S* is the contact surface.

3.3. Mach 3 flow over a forward facing step

The third test problem in validating the DD-QDS code is the Mach 3 flow over a forward facing step in a high speed two-dimensional wind tunnel. This test problem was introduced by Emery [22] and has been used in several studies including Woodward and Colella in testing a few numerical schemes [23] and Keats and Lien who used a Godunov scheme [24]. Fig. 5 shows the geometry of the problem with a uniform Mach 3 flow over a step which is located 0.6 unit length from the inlet of the tunnel. The simulated gas was an ideal gas with a ratio of specific heats of 1.4 and a gas constant of $R = 1.0$. Initially, the flow is uniform everywhere with density of 1.4, pressure of 1.0, and velocity of 3.0. The inlet boundary remains as the initial flow condition while the outlet boundary condition was extrapolated from the adjacent flow field cells. Reflecting wall boundary conditions are applied along the walls of the tunnel.

The simulation was conducted with the second order DD-QDS codes by using 4 velocity bins per coordinate direction on a uniform grid and the MINMOD slope limiter in calculating properties gradients. The variable time step scheme was used so the maximum kinetic CFL number in the simulation domain was 0.5 with 200 square cells along the height of the tunnel.

The simulation result is compared to that of the second order Godunov method employed by Keats and Lean on an adaptively refined mesh [24]. Fig. 6 shows a comparison of density contour at 4 s between the results of Keats and Lien's Godunov scheme and the DD-QDS scheme. The comparison shows the DD-QDS code has captured the flow field features such as the Mach stem and rarefaction fan around the corner of the step with results very close to that of Keats and Lien's Godunov scheme. The shock positions on the walls also show close agreement.

The DD-QDS simulation was conducted on a single desktop computer with 3.00 GHz Intel Core 2 Duo CPU E6850 processor and 4 GB of RAM. The simulation consumed 22 min to compute 4.0 s flow. By comparison, the same problem was simulated using the second order True Directional Equilibrium Flux Method (TDEFM) [20,25] and a Riemann solver on a single laptop computer with 1.73 GHz Intel dual core T2250 processor and 2 GB of RAM [5]. The TDEFM required 201 min to compute 4.0 s of flow while the Riemann solver required 77 min. Although the DD-QDS simulation was carried out on a machine with about double the speed, the computational speed-up is significant and the DD-QDS computation would take less than half time on the same machine, than the other two methods.

4. PP–CVD simulations

The DD-QDS solver is used to simulate the reactor flow field for the gas injected PP–CVD process. Two cases were simulated at two different operating pressure conditions as described in Table 1. In both simulations, ideal Helium gas at choked inlet flow conditions is injected into the reactor though an orifice. At the start of

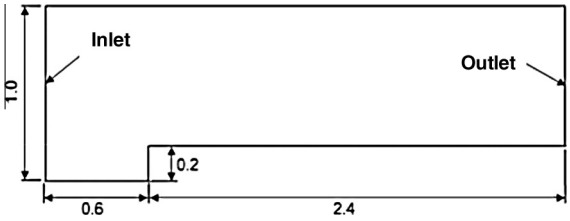

Fig. 5. Geometry and boundary conditions for the simulation of Mach 3 flow over a forward facing step.

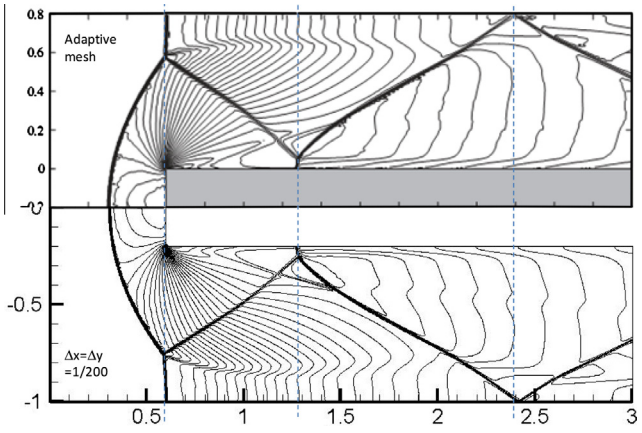

Fig. 6. Comparison of density contour at 4 s for Mach 3 flow over a forward facing step in a wind tunnel between results from Keats and Lien's Godunov scheme (Top, taken from [24]) and DD-QDS scheme (bottom).

injection, the gas in the reactor is stationary. A constant evacuation volumetric flow rate is used as the outflow conditions. Specular reflecting walls were used for all wall and substrate surfaces. Both simulations were carried out on a desktop computer with 3.00 GHz Intel Core 2 Duo CPU and 4 GB of RAM using 312,744 uniform square cells with 0.25 mm cell size.

Fig. 7 shows the reactor geometry and boundary conditions used for both cases.

4.1. Case I: 1 Pa initial reactor pressure

4.1.1. Case I: Injection phase

Fig. 8 shows the density contours (left) and the pressure contours (right) plotted on natural logarithm scale. They show the development of an under-expanded jet during the first 4 ms of the injection phase. It is noted that the under-expanded jet with wide shock structure develops during the injection phase. These results show the same shock structure and flow development found in DSMC simulations of Cave [10,26]. The DD-QDS results have higher resolution and of course much better computational efficiency. The contour plots in Fig. 8 show a wide initial bow shock

Table 1
Simulation conditions for **PP–CVD** flow field simulations using DD-QDS.

	Case I	Case II
Supply pressure, P_s	10 kPa	40 kPa
Pulse range, $P_{min} \rightarrow P_{max}$	1 Pa $\rightarrow \sim$100 Pa	1 kPa $\rightarrow \sim$5 kPa
Injection time, t_i	0.1 s	
Supply temperature, T_s	293 K	
Initial temperature, T_i	293 K	
QDS velocity bin, N	Four per coordinate direction	
Simulation time step, Δt	Variable time step with maximum CFL < 0.5	
Slope limiter	MINMOD	

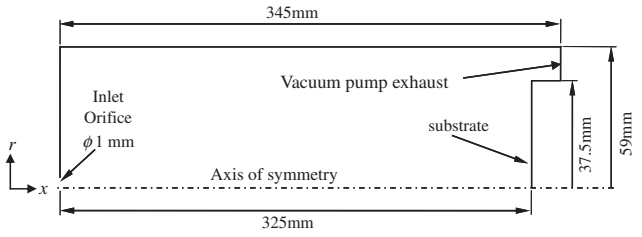

Fig. 7. Schematic of PP–CVD reactor geometry.

at the exit of the inlet orifice, followed by the development of a shock wave pattern, evolution of the shear layer and the formation of a Mach disc during the unsteady flow development period. After 4.0 ms, a quasi-steady under-expanded jet structure impinges onto the substrate. The formation and evolution of constantly changing expansion and compression waves, which are also seen in the numerical studies performed using the space–time conservation element solution element (CE/SE) method on unsteady jet flows from a rocket nozzle [27], are captured by the QDS solver. This demonstrates the capability of the QDS solver in modelling unsteady flow phenomena at low computational cost.

One of the important assumptions in the QDS method is that thermal equilibrium is established locally within each computational cell by the end of the time step, allowing the molecular velocity distribution to be approximated with the Maxwell–Boltzmann distribution. In an expanding flow, generally, local thermal equilibrium cannot be maintained when the molecular collision rate becomes so low that continuum breakdown occurs. To investigate the validity of local equilibrium assumption, the gradient length local (*GLL*) Knudsen number proposed by Boyd et al. [28] was calculated at the simulation times of 0.5 ms and 4.0 ms after the start of injection. At 0.5 ms, the Mach disc position was stabilized in the flow field while the flow developed into quasi-steady state at 4.0 ms. The gradient length local Knudsen number Kn_{GLL} is a continuum breakdown parameter which compares the local mean free path to the scale length of any macroscopic property gradient:

$$Kn_{GLL} = \frac{\lambda}{Q}|\nabla Q| \tag{4.1}$$

where λ is the local mean free path, Q is the flow property (e.g. density, translational temperature or velocity magnitude) and ∇Q the spatial gradient of the flow property. Boyd et al. [28] proposed that continuum breakdown occurs when Kn_{GLL} is greater than 0.05. Hence, $(Kn_{GLL})_\rho < 0.05$, or $\log_e[(Kn_{GLL})_\rho] < -3.0$, is taken as the condition that continuum breakdown does not occur, i.e. the local density gradient is not high enough to transport the gas molecules downstream before thermal equilibrium is re-established within the computational cell, given that the computational cells are always larger than the mean free path. Fig. 9 shows the contours of $(Kn_{GLL})_\rho$ plotted on natural logarithm scale at the simulation times of 0.5 ms and 4.0 ms, respectively, for Case I. It is noted that $\log_e[(Kn_{GLL})_\rho] < -3.0$ throughout the flow field indicating that the continuum assumption is valid in Case I.

The validity of the thermal equilibrium assumption may also be tested by considering the average time between molecular collisions estimated by:

$$t_{col,avg} = \frac{\lambda}{v_{th,avg}} \tag{4.2}$$

where $v_{th,avg}$ is the average translational thermal speed given by:

$$v_{th,avg} = \sqrt{\frac{3kT}{m}} \tag{4.3}$$

where k is the Boltzmann's constant and m is the mass of an individual molecule. Titov and Levin [29] found, in collision-limited DSMC, that two collisions per time step per particle are sufficient for the computed non-equilibrium distribution to relax to one differing negligibly from the corresponding Maxwell–Boltzmann equilibrium distribution. In the present analysis, the average time between molecular collisions is compared to the computational time step, Δt. Fig. 10 shows the contours of the $\Delta t/t_{col,avg}$ plotted on natural logarithm scale at the simulation times of 0.5 ms and 4.0 ms, respectively, for Case I. The equilibrium assumption may be considered valid where $\Delta t/t_{col,avg} \geqslant 2$ or $\log_e(\Delta t/t_{col,avg}) \geqslant 0.69$.

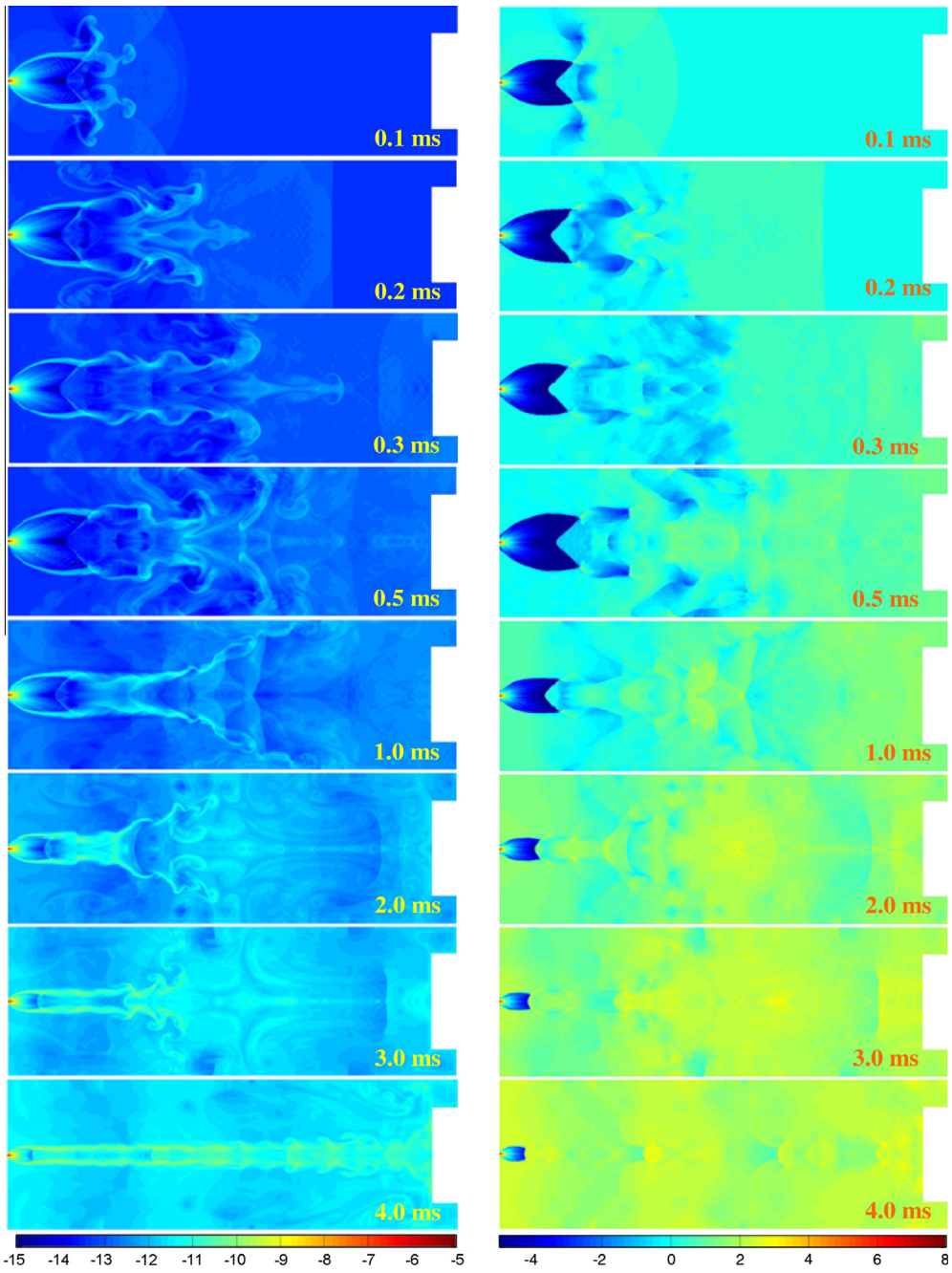

Fig. 8. $\log_e$(density) contour (left) and $\log_e$(pressure) contour (right) for the unsteady flow development of an under-expanded jet in the PP–CVD reactor at Case I conditions during first 4 ms of the injection phase.

It is noted that the condition of $\log_e(\Delta t/t_{col,avg}) \geqslant 0.69$ is not satisfied anywhere in Case I either at $t = 0.5$ ms or $t = 4.0$ ms, except near the orifice exit. This indicates the computational time step used in the simulation is much smaller than the average molecules' collision time preventing the sufficient relaxation of the molecules. Therefore, the DD-QDS solver may not be able to calculate such non-equilibrium flow accurately. However, the similarity between the present results and the DSMC results of Cave [10,26] suggests QDS is able to provide a promising approximation of the flow field at 1 Pa initial pressure condition.

4.1.2. Case I: Pump down phase

The pump down phase of the PP–CVD operating cycle at Case I conditions was also simulated. The reactor pressure at the end of the injection phase is estimated to be 100 Pa based on experience with such reactors. Fig. 11 shows the density contours (left) and the pressure contours (right) plotted on a natural logarithm scale. They show the dissipation of the quasi-steady jet after the inlet nozzle shuts at 0.1 s. It can be observed that the jet structure has dissipated during the first 0.5 ms of the pump down phase. The resulting flow field is rather uniform for the remaining pump-down process. Information on the jet formation and dissipation, and the structure of the flow field near the substrate, is useful for the design and choice of operating conditions for the PP–CVD process.

The ratio of the simulation time step to the average time between molecular collisions was calculated to estimate the number of collisions per time step per velocity bin within a computational

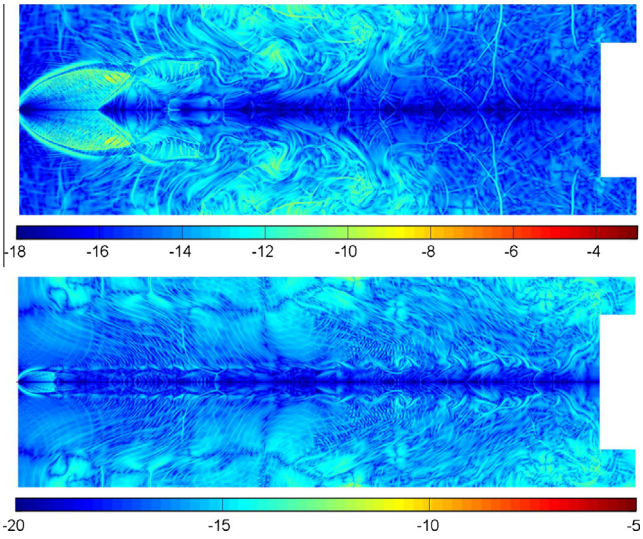

Fig. 9. $\mathrm{Log_e}[(Kn_{GLL})_\rho]$ contours at 0.5 ms (top) and 4 ms (bottom) at Case I conditions.

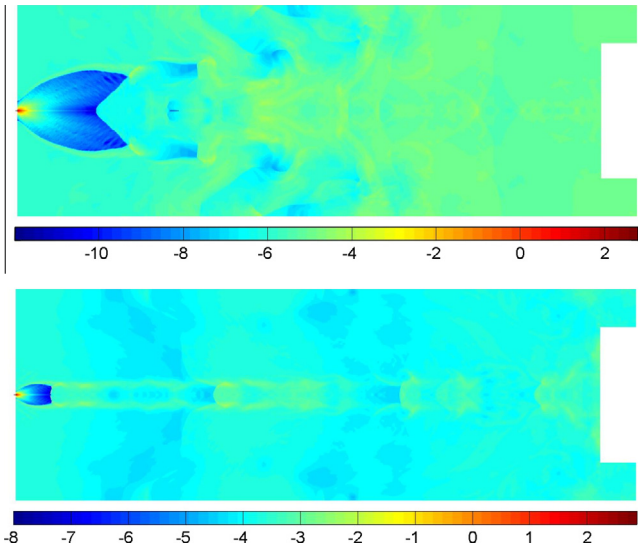

Fig. 10. $\mathrm{Log_e}(\Delta t/t_{col,avg})$ contours at 0.5 ms (top) and 4 ms (bottom) at Case I conditions.

cell. Fig. 12 shows the contours of the $\log_e(\Delta t/t_{col,avg})$ at 0.10001 s (10 μs after the end of injection) and 0.1001 s, respectively, during the pump-down phase for Case I. Fig. 12 shows that the condition $(\Delta t/t_{col,avg}) \geqslant 2$ or $\log_e(\Delta t/t_{col,avg}) \geqslant 0.69$ i.e. two collisions per time step per velocity bin is not achieved during the pump-down phase simulation in Case I.

Fig. 13 shows the log scaled contours of the of the gradient length local Knudsen number based on density at the simulation times of 0.10001 s and 0.1001 s, respectively, for Case I. As discussed above, Boyd et al. [28] suggested that continuum breakdown occurs at $Kn_{GLL} > 0.05$. The contour plots in Fig. 13 shows that $(Kn_{GLL})_\rho$ is overall less than 0.05 (or $\log_e(Kn_{GLL})_\rho < -3$) soon after the inlet jet was shut down. Therefore, although the number of collisions was low and the two collisions per time step per velocity bin condition is not satisfied, the local density gradient within the computational cell was not high enough to transport the gas downstream before thermal equilibrium condition was established. Hence, the assumption that equilibrium is re-established locally in each time step in the current QDS scheme is partially justified for PP–CVD process during the pump-down phase.

4.2. Case II: 1 kPa initial reactor pressure

4.2.1. Case II: Injection phase

Fig. 14 shows the density contours (left) and the pressure contours plotted on a natural logarithm scale (right) of the simulation results for Case II conditions during the first 4 ms of the injection phase. Due to the higher initial reactor pressure, the density gradient between the inlet and the initial reactor condition is relatively small, resulting in lower rates of diffusion and pressure driven flow radially from the high concentration regions, at the inlet and on the centreline of the reactor, to the outer radius regions, and consequently lower rates of mass transport radially outwards, compared to Case I. Hence, the under-expanded jet has a much narrower shock structure during the injection phase, compared to Case I. Again, complicated flow phenomena such as the initial bow shock at the exit of the inlet orifice, the shear layer evolution and eventual Mach disc formation, during the unsteady flow development period were captured in clear detail. The flow field eventually becomes quasi-steady at about 3 ms.

Fig. 15 shows the contours of $(Kn_{GLL})_\rho$ plotted on natural logarithm scale at the simulation times of 0.5 ms and 4.0 ms, respectively, of the simulation results for Case II. It is shown that $\log_e[(Kn_{GLL})_\rho] < -5.0$ throughout the flow field at all time. Hence, it may be safely assumed that continuum breakdown does not occur in Case II and the local density gradient within the computational cell was not high enough to transport the gas downstream before local thermal equilibrium is re-established after each time step. This justifies the assumption of local thermal equilibrium in the present QDS scheme at initial reactor pressure of 1 kPa.

The ratio of the simulation time step to the average time between molecular collisions was then calculated for Case II. Fig. 16 shows the contours of $\Delta t/t_{col,avg}$ plotted on a natural logarithm scale at the simulation times of 0.5 ms and 4.0 ms, respectively, for Case II. From Fig. 16, it is observed that $\log_e(\Delta t/t_{col,avg}) \geqslant 0.69$ (or $\Delta t/t_{col,avg} \geqslant 2$) in most regions except a small highly supersonic region upstream behind the Mach disc. However, this region is unlikely to have a significant effect on the flow field, especially near the substrate region which is the region of interest in the simulation. Hence, in general, this suggests that there are at least two successive molecular collisions per computational time step in most regions of the flow field providing insignificant difference between the actual physical non-equilibrium distribution and the Maxwellian equilibrium distribution. This again reasonably justifies the equilibrium assumption in the present QDS scheme in simulating the flow field of Case II.

4.2.2. Case II: Pump down phase

The pump-down phase of the PP–CVD operating cycle at Case II conditions was also simulated with the reactor pressure at the end of the injection phase is estimated to be 5 kPa. Fig. 17 shows the density contours (left) and the pressure contours (right) plotted on natural logarithm scale. Similar to that of Case I, the jet structure also dissipates rapidly in about 0.5 ms, after the inlet jet has been shut off at 0.1 s, followed by a considerably uniform flow field in the remaining pump-down process.

The validity check on the thermal equilibrium assumption in the current QDS scheme was again performed for the Case II pump-down phase simulation. Fig. 18 shows the log scaled contours of the of the gradient length local Knudsen number based on density at the simulation times of 0.10001 s and 0.1001 s, respectively. As discussed above, it can be considered that continuum breakdown does not occur for $(Kn_{GLL})_\rho < 0.05$ or $\log_e(Kn_{GLL})_\rho < -3$. The contour plots in Fig. 18 shows that $\log_e(Kn_{GLL})_\rho$ is overall less than -5, permitting the continuum assumption to be valid in the flow field based on $(Kn_{GLL})_\rho$. The local density gradient within the computational cells is not high enough to transport the

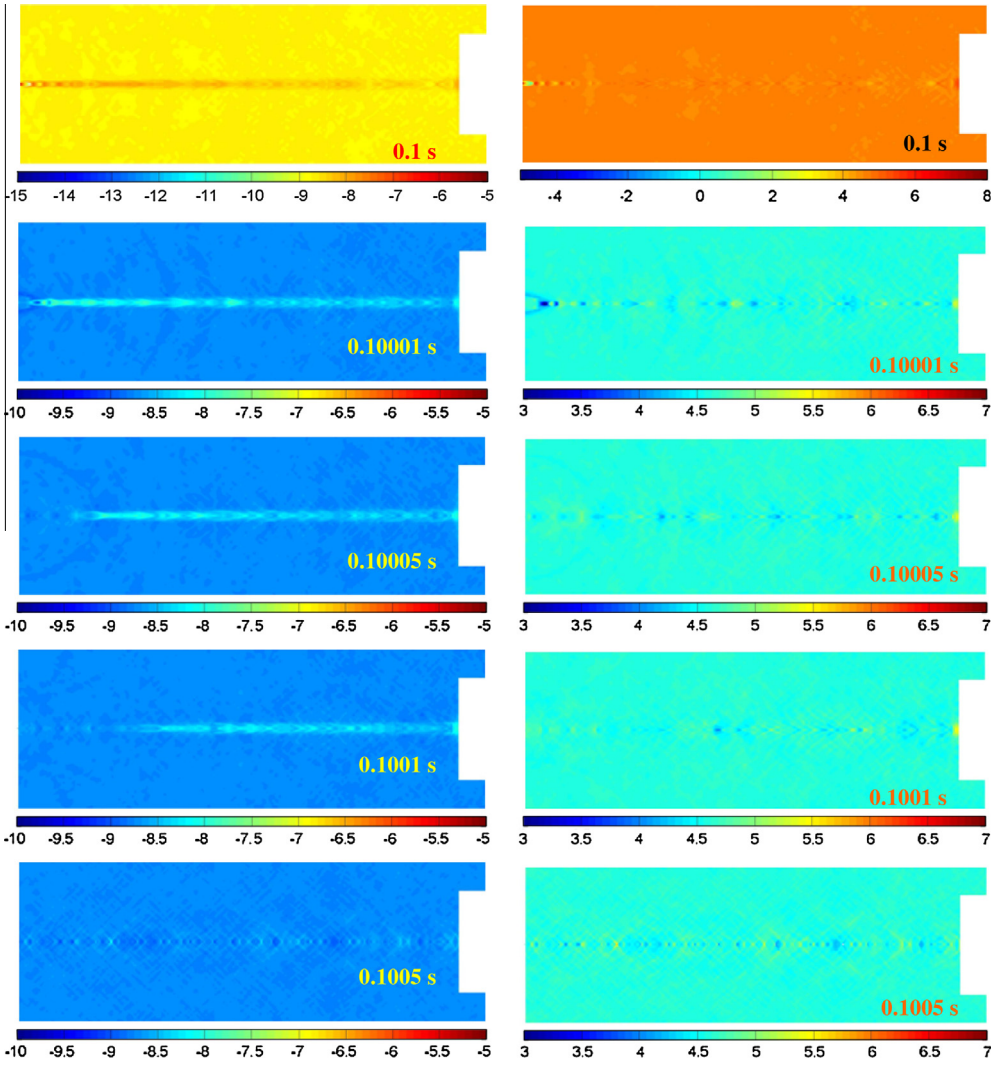

Fig. 11. Log_e(density) contour (left) and log_e(pressure) contour (right) after inlet orifice closes (at 0.1 s) in a PP–CVD reactor at Case I conditions.

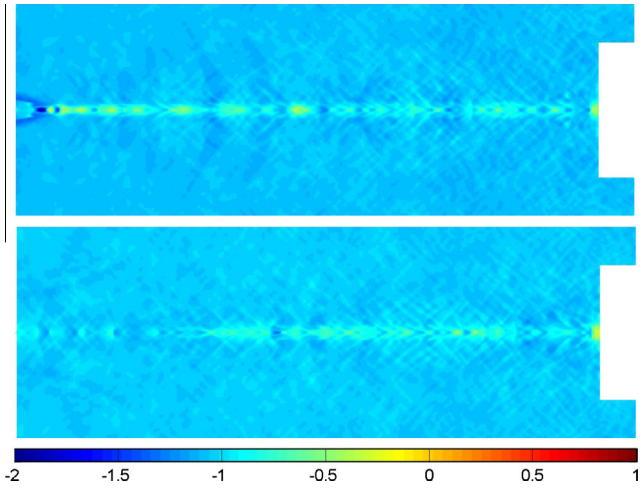

Fig. 12. $\text{Log}_e(\Delta t/t_{col,avg})$ contours at 0.10001 s (top) and 0.1001 s (bottom) at Case I conditions.

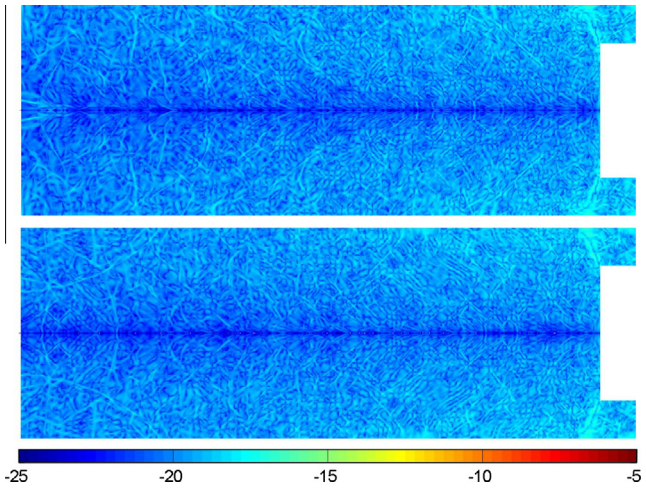

Fig. 13. $\text{Log}_e(Kn_{GLL})_\rho$ contours at 0.10001 s (top) and 0.1001 s (bottom) at Case I conditions.

gas downstream before thermal equilibrium condition is re-established locally in within one time step.

The ratio of the simulation time step to the average time between molecular collisions, $(\Delta t/t_{col,avg})$ is shown in Fig. 19 at 0.10001 s and 0.1001 s, respectively, during the pump-down phase for Case II. As the condition of $(\Delta t/t_{col,avg}) \geqslant 2$ or $\text{log}_e(\Delta t/t_{col,avg}) \geqslant 0.69$ is used to estimate whether there are enough

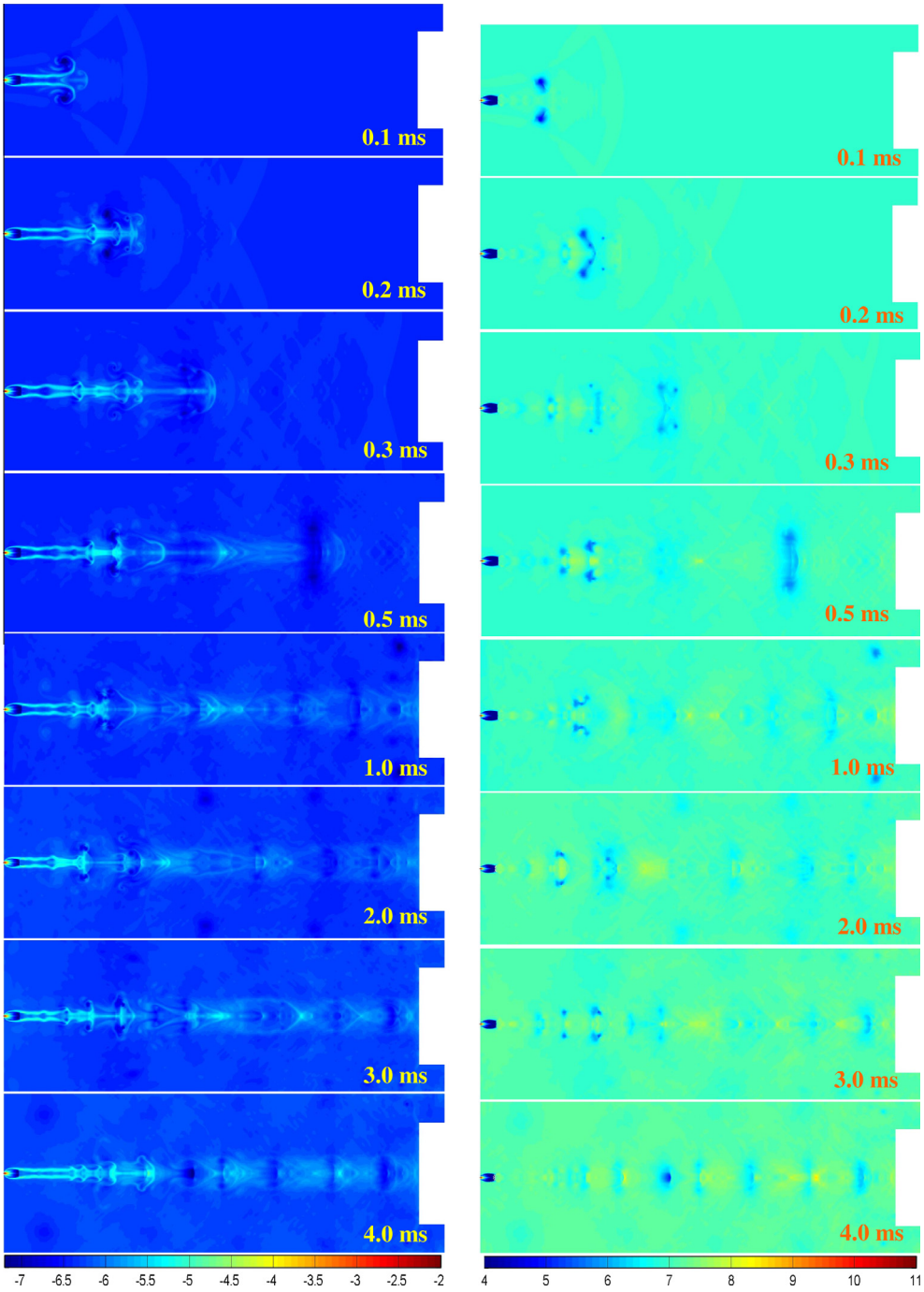

Fig. 14. Log_e(density) contour (left) and $\log_e$(pressure) contour (right) for the unsteady flow development of an under-expanded jet in a PP–CVD reactor at Case II conditions during first 4 ms of the injection phase.

collisions per time step per velocity bin to bring the molecular velocity distribution acceptably close to the Maxwellian equilibrium distribution, Fig. 19 shows $\log_e(\Delta t/t_{col,avg}) \geqslant 2.5$ in the simulation everywhere.

4.3. Discussion

4.3.1. PP–CVD reactor flow field uniformity

Figs. 8 and 14 have shown that the time required for the quasi-steady structure of the jet to establish is 4 ms in Case I and 3 ms in Case II. The time required for the quasi-steady structure to dissipate is about 0.5 ms for both cases as noted from Figs. 11 and 17. Knowledge of these times, not previously available, enables judicious choice of the injection pulse length and repetition frequency. Besides, comparing Case I and Case II it is seen that the high density gradient between the inlet and the bulk of the reactor causes higher rates of mass transport radially outwards in Case I. Hence the lower initial reactor pressure achieves a more uniform distribution of precursor solution before being transported to the substrate region.

The simulation results in both Case I and II shows that the flow field developed into a quasi-steady under-expanded jet structure, which impinges onto the substrate during the injection phase of the PP–CVD process. The impingement of the jet with its high

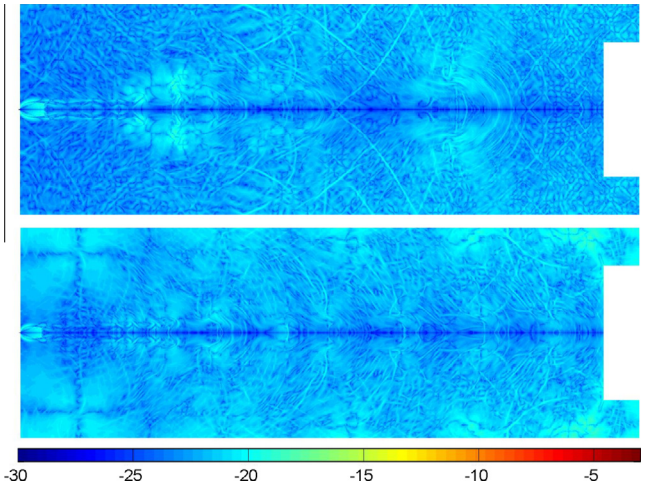

Fig. 15. $\mathrm{Log_e}[(Kn_{GLL})_\rho]$ contours at 0.5 ms (top) and 4.0 ms (bottom) at Case II conditions.

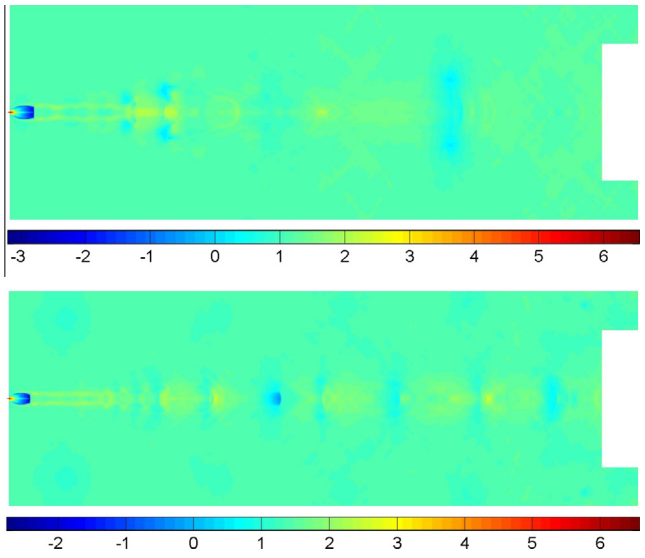

Fig. 16. $\mathrm{Log_e}(\Delta t/t_{col,avg})$ contours at 0.5 ms (top) and 4 ms (bottom) at Case II conditions.

density core is undesirable for CVD due to the formation of a developing boundary layer on the substrate in this reactor configuration which results in non-uniformity of the mass flux onto the substrate. Such non-uniformity of molecular impingement on the substrate surface, if sustained, would result in non-uniform deposition of the precursor onto the substrate. However, PP–CVD reactors are typically operated with short injection pulses, which comprise a small fraction of the total cycle time during which deposition may occur. Film deposition is thought to continue for some considerable time after the gas supply is cut off and the jet structure has dissipated, when the flow field is more uniform. This encourages uniform film deposition on the substrate surface since the majority of the actual deposition process occurs during the pump down phase. Hence, the non-uniformity of deposition incurred during the injection phase has a limited impact on the uniformity of the final deposited film. On the other hand, the narrow jet impingement on the centre of the substrate toward the end of the injection phase also suggests that placement of the substrate at the centre of the reactor should be avoided whenever possible.

4.3.2. Numerical diffusion in the QDS scheme

The above simulation results have also demonstrated some of the problems inherent in using QDS throughout the whole PP–CVD flow field. There are two features of the QDS scheme limit its accuracy in low Mach number flows. One of the issues in the QDS scheme is the separation of collision and streaming that leads to excessive numerical diffusion of momentum [30]. Consequently, this results in high artificial viscosity of the gas when the grid spacing is larger than the mean free path. The similarity of the present results with the test cases presented above and the DSMC of Cave [10,26] suggests this does not affect the simulation of high Mach number flows or the low pressure PP–CVD reactors simulated here, wall of which are inertially dominated. Nevertheless the artificially high viscosity should be borne in mind when interpreting future QDS results. A numerical scheme which achieves both realistic viscosity of the simulated gas and the computational efficiency of QDS would have interesting applications.

The numerical diffusion in the QDS scheme is in proportion to the cell size [30]. For the particular PP–CVD reactor simulation of interest, simulation with cell size of $\Delta x = 2.5 \times 10^{-4}$ m requires 4 h for 1 ms flow time. Reducing the cell size to $\Delta x = 1.25 \times 10^{-4}$ m halves the viscosity of the simulated gas, and increases the computational time to 72 h to compute 1 ms flow time. For the purpose of exploring PP–CVD reactor design, the speed of simulation is prioritised over the quantitative accuracy of the flow field computed.

Fig. 20 shows the comparison of $\log_e$(density) contour plots between the simulation results with grid size of $\Delta x = 2.5 \times 10^{-4}$ m and $\Delta x = 1.25 \times 10^{-4}$ m. During the injection phase of the PP–CVD process, the flow field develops into a quasi-steady state after the first 4 ms in the 1 s injection phase. The flow remains in quasi-steady state for about 99.6% of the injection time. From Fig. 20, it shows that halving the grid size, which consequently halving the viscosity, has little effect on the flow field, especially after the quasi-steady jet was developed.

Fig. 21 shows the accumulated number of computational velocity bins colliding with the substrate face for three different cell sizes used throughout the simulation time of 3 ms. This quantity is named accumulated mass on substrate or AMOS, as when it is multiplied by a factor related to the probability of deposition and thermal decomposition, it determines the mass of deposited material which remains on the substrate when the reactor is used for manufacturing coatings. As shown in Fig. 21, the difference in the number of bins colliding with the substrate wall between runs with a cell size of $\Delta x = 2.5 \times 10^{-4}$ m and $\Delta x = 1.25 \times 10^{-4}$ m is much less compared to that between runs with a cell size of $\Delta x = 5.0 \times 10^{-4}$ m and $\Delta x = 2.5 \times 10^{-4}$ m. From Fig. 21, it is also noted that AMOS increases linearly with the radius since the annular area of the computational cell normal to the axial direction is linearly proportional to the radius. To characterise the uniformity of the flow field near the substrate surface, AMOS per unit cell area normal to the axial direction is calculated and plotted as shown in Fig. 22. It should be noted that non-uniformity in AMOS per area in Fig. 22 is within expectation since the results are plotted for only the first 3 ms of the injection phase, which is a very small fraction of the whole deposition cycle. Regardless, the difference in the AMOS per area between runs with a cell size of $\Delta x = 2.5 \times 10^{-4}$ m and $\Delta x = 1.25 \times 10^{-4}$ m is less than that between runs with a cell size of $\Delta x = 5.0 \times 10^{-4}$ m and $\Delta x = 2.5 \times 10^{-4}$ m. Hence, a cell size of $\Delta x = 2.5 \times 10^{-4}$ m is used to allow speedy computation with reasonable quantitative accuracy. Although the quantitative accuracy reduces with the high value of numerical viscosity, the qualitative flow field phenomena especially the shock position and structure are not jeopardised. In fact, for the purpose of exploring PP–CVD reactor design and selecting operating conditions, the qualitative simulation result is sufficient.

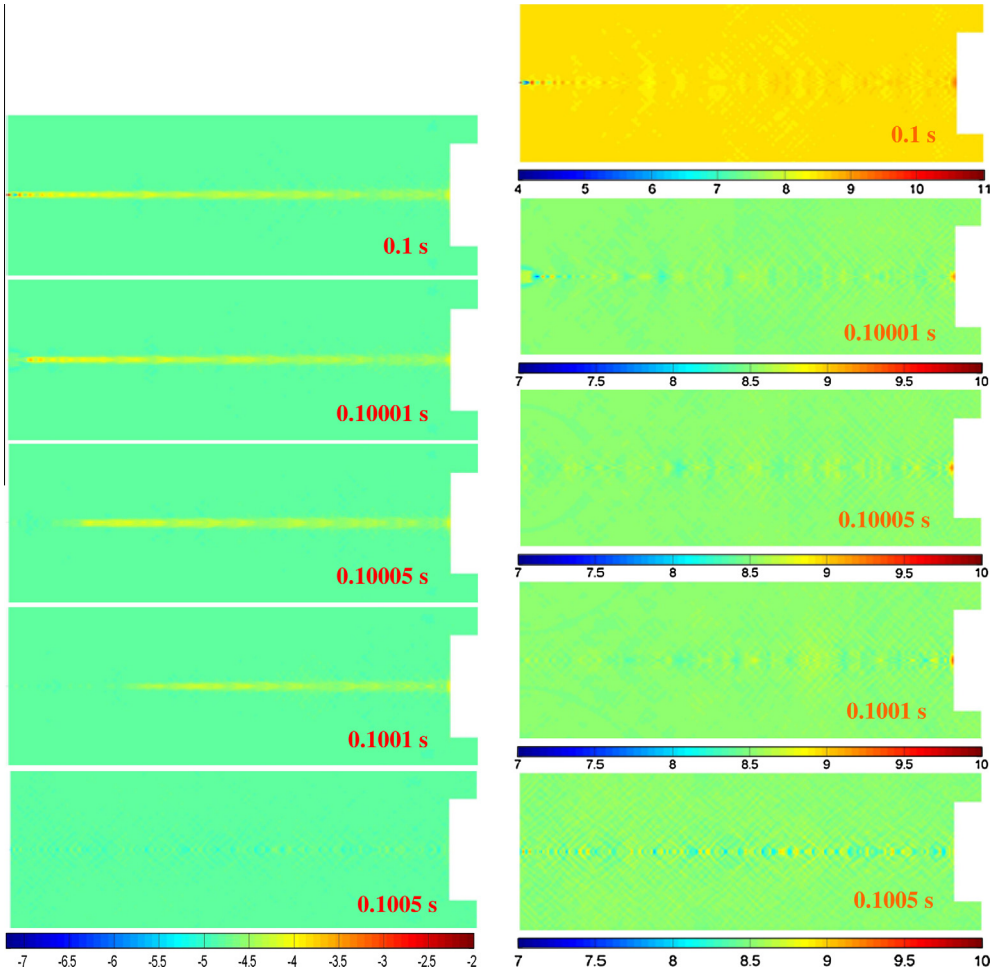

Fig. 17. Log_e(density) contour (left) and log_e(pressure) contour (right) after inlet orifice closes (at 0.1 s) in a PP–CVD reactor at Case II conditions.

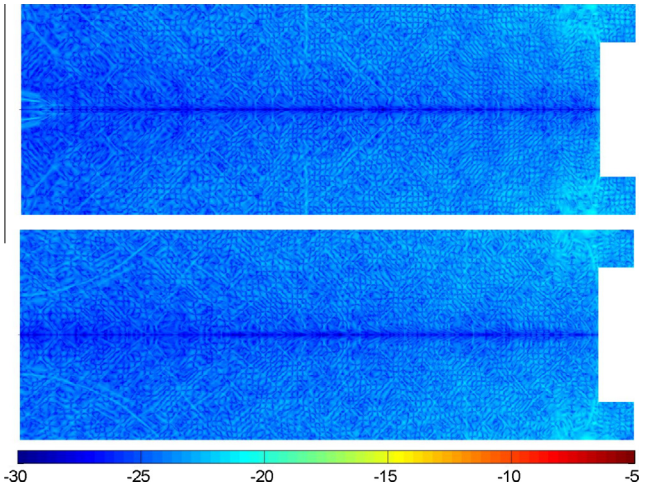

Fig. 18. $\text{Log}_e(Kn_{GLL})_\rho$ contours at 0.10001 s (top) and 0.1001 s (bottom) at Case II conditions.

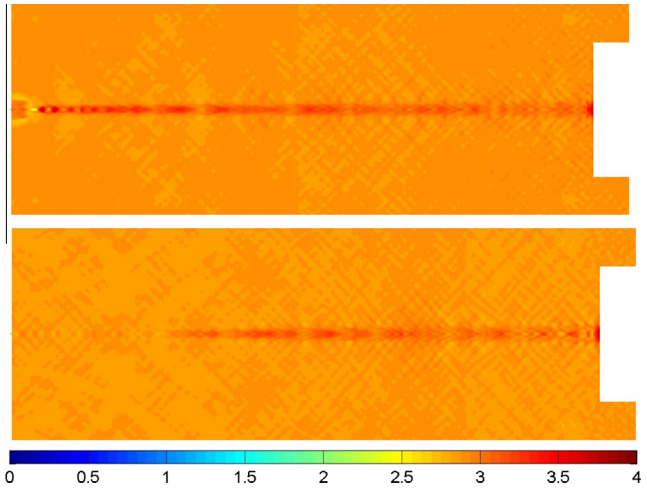

Fig. 19. $\text{Log}_e(\Delta t/t_{col,avg})$contours at 0.10001 s (top) and 0.1001 s (bottom) at Case II conditions.

4.3.3. Limitation of the QDS scheme in PP–CVD flow simulation

Another important assumption in the QDS is Maxwell–Boltzmann equilibrium distribution of molecular velocities. The validity of this assumption may be checked by calculating the gradient length local Knudsen number and average number of collisions per time step.

The local thermal equilibrium assumption precludes the QDS scheme from use in simulating highly rarefied flows. Due to the larger mean free path of the molecules in highly rarefied low pressure flow, the gas may not reach equilibrium condition during the computational time step used. The limitation of the DD-QDS scheme is investigated by utilising the gradient length local

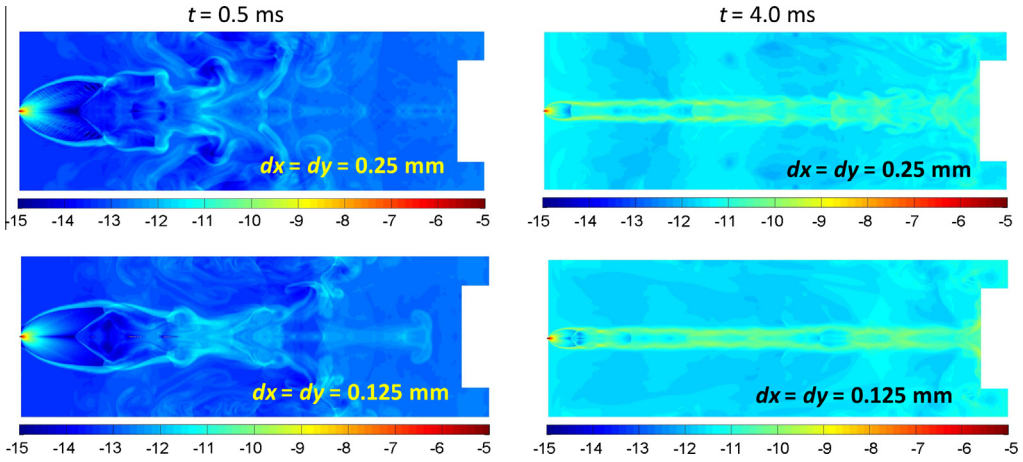

Fig. 20. Comparison of $\log_e$(density) contour plots for the PP–CVD simulations with grid sizes of 0.25 mm and 0.125 mm.

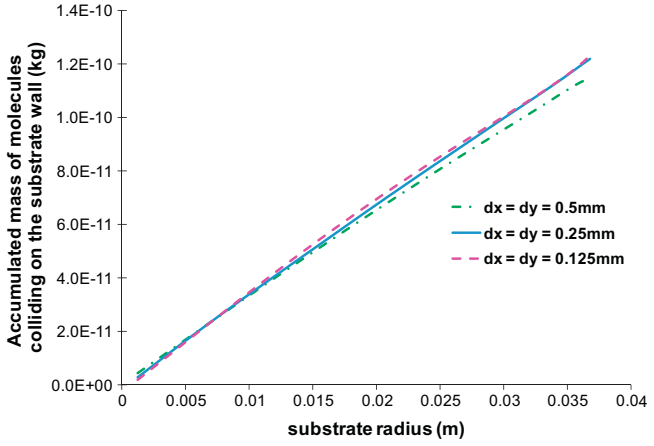

Fig. 21. Accumulated mass of molecules colliding onto the substrate wall (AMOS) from simulations of three different cell sizes.

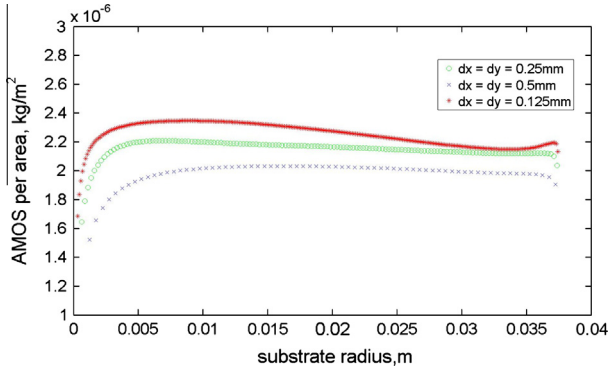

Fig. 22. Accumulated mass of molecules collide onto the substrate wall (AMOS) per substrate annular area from simulations of three different cell sizes.

Knudsen number $(Kn_{GLL})_\rho$ and the ratio of computational time step to the average time between molecular collisions $\Delta t/t_{col,avg}$.

A series of simulations at various minimum reactor pressures have been carried out in order to estimate the limit of the DD-QDS scheme in simulating low pressure flow with justified assumption of local thermal equilibrium. As seen from Figs. 8 and 15, the threshold of $(Kn_{GLL})_\rho$ is met for the flow pressure as low as 1 Pa, which is the lowest possible rector pressure in the current experimental PP–CVD reactor. However, the calculation of $\Delta t/t_{col,avg}$ shows that the low frequency of molecular collisions with 1 Pa initial reactor pressure condition hinders the restoration of local thermal equilibrium. Hence, simulations of the same PP–CVD flow condition, changing only the reactor initial pressure of 1 Pa, 100 Pa, 200 Pa, 300 Pa, and 400 Pa, have been conducted. Fig. 23 shows the $\log_e(\Delta t/t_{col,avg})$ contours of the PP–CVD reactor flow simulations with initial pressures of 200 Pa, 300 Pa and 400 Pa.

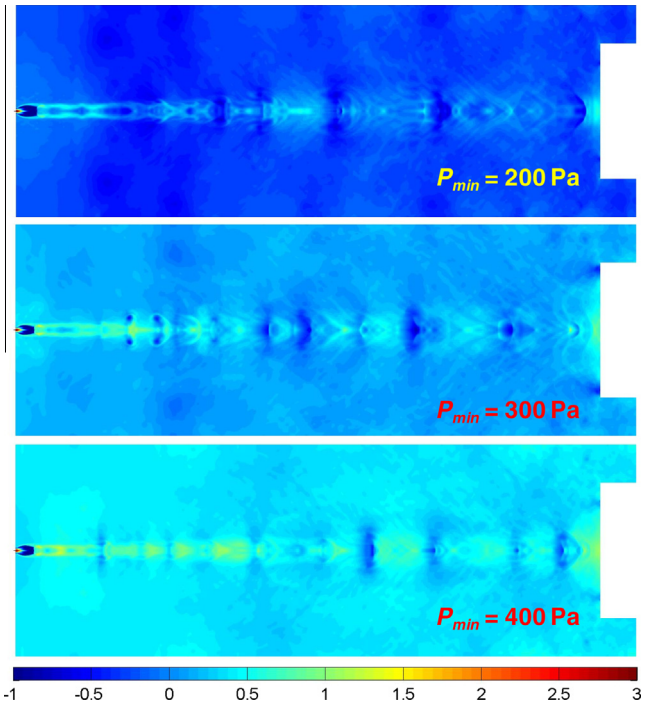

Fig. 23. $\log_e(\Delta t/t_{col,avg})$ contours at 4 ms of the PP–CVD reactor flow simulations with initial pressures of 200 Pa (top), 300 Pa (middle) and 400 Pa (bottom).

Since $(Kn_{GLL})_\rho \leqslant 0.05$ has been met for runs with $P_{min} = 1$ Pa as shown in the results from Case I above, it requires only to check if $\Delta t/t_{col,avg} \geqslant 2$ in order to set a limit of the DD-QDS scheme in simulating PP–CVD flows. From Fig. 23, it can be seen that $\Delta t/t_{col,avg} \geqslant 2$, or $\log_e(\Delta t/t_{col,avg}) \geqslant 0.69$ has been just met in the simulation with $P_{min} = 400$ Pa in most regions but not for simulations with P_{min} lower than this. Thus, it can be considered that the

Table 2
Minimum and maximum values of $(Kn_{GLL})_\rho$ and Kn at 4 ms for the series of **PP–CVD** reactor flow simulation conducted at different P_{min} with diameter of the reactor $D_{reactor}$ = 0.118 m.

P_{min} (Pa)	$(Kn_{GLL})_\rho$		Mean free path, λ		Kn ($\lambda/D_{reactor}$)	
	Min	Max	Min	Max	Min	Max
1	8.892e−17	5.891ev04	2.582e−06	6.627e−01	2.188e−05	5.61591
100	1.630e−19	9.376e−07	2.582e−07	9.680e−04	2.188e−06	0.00820
200	4.809e−19	3.487-07	2.582e−07	4.563e−04	2.188e−06	0.00387
300	1.926e−19	3.694e−07	2.582e−07	2.510e−04	2.188e−06	0.00213
400	3.295e−20	1.857e−07	2.582e−07	1.936e−04	2.188e−06	0.00164

DD-QDS is able to produce numerical solution with reasonably accuracy to the PP–CVD flow with P_{min} = 400 Pa or above.

The gradient length local Knudsen number $(Kn_{GLL})_\rho$ and the Knudsen number Kn are also calculated for the series of simulations conducted and tabulated in Table 2 as below. This is done in order to determine the limit of the DD-QDS scheme that satisfy both $(Kn_{GLL})_\rho$ and $\Delta t/t_{col,avg}$ conditions as mentioned above. By noting the maximum values of $(Kn_{GLL})_\rho$ and Kn for the simulation with P_{min} = 400 Pa, it becomes possible to set a limit within which the DD-QDS scheme that the simulation results are considered acceptably valid for low pressure flows with $(Kn_{GLL})_\rho \leqslant 1.857 \times 10^{-7}$ or $Kn \leqslant 0.00164$. This range of Knudsen number is the generally accepted value for continuum flow.

5. Conclusions

The axisymmetric, second-order, directional decoupled QDS scheme has been used to simulate the flow field in the highly unsteady low pressure flow of the PP–CVD process. The DD-QDS simulation results agree well to that of the previously performed simulation using the DSMC method. DD-QDS provides a good approximation of the flow field with excellent computational efficiency as well as simplicity in usage. The validity of the local equilibrium assumption has been tested. The limit of the DD-QDS scheme in simulating the low pressure PP–CVD flow has been determined. In addition, the time taken to establish and dissipate the quasi-steady jet structure has also been determined. This information is essential for the design of the PP–CVD reactors and operating cycles.

Acknowledgements

We would like to thank the New Zealand Foundation for Research, Science and Technology (FRST) International Investment Opportunity Fund (IIOF) for the financial support of this research through Grant No. UOCX070210 and the National Science Council of Taiwan for the support of the corresponding author, Prof. J.-S. Wu, through Grant No. 96-2628-E-009-136-MY3 and Dr. M.R. Smith through Grant No. 99-2221-E-492-005-MY3. This research was conducted as part of Chin Wai Lim's Ph.D. project under the sponsorship of Universiti Tenaga Nasional, Malaysia. Dr. M.R. Smith would also like to acknowledge Dr. Michael Macrossan and Prof. Gary Cheng for their contributions to this work.

References

[1] Bird GA. Approach to translational equilibrium in a rigid sphere gas. Phys Fluids 1963;6:1518–9.
[2] Pullin DI. Direct simulation methods for compressible inviscid ideal-gas flow. J Comput Phys 1980;34:231–44.
[3] Albright BJ, Daughton W, Lemons DS, Winske D, Jones ME. Quiet direct simulation of plasmas. Phys Plasmas 2002;9:1898–904.
[4] Albright BJ, Lemons DS, Jones ME, Winske D. Quiet direct simulation of Eulerian fluids. Phys Rev E 2002;65:055302.
[5] Smith MR, Cave H, Wu JS, Jermy MC, Chen YS. An improved quiet direct simulation method for Eulerian fluids using a second-order scheme. J Comput Phys 2009;228:2213–24.
[6] Versteeg VA, Avedisian CT, Raj R. Metalorganic chemical vapor deposition by pulsed liquid injection using an ultrasonic nozzle: titanium dioxide on sapphire from titanium(IV) isopropoxide. J Am Ceram Soc 1995;78:2763–8.
[7] Cave HM, Krumdieck SP, Jermy MC. Development of a model for high precursor conversion efficiency pulsed-pressure chemical vapor deposition (PP–CVD) processing. Chem Eng J 2008;135:120–8.
[8] Krumdieck SP, Cave HM, Baluti S, Jermy M, Peled A. Expansion transport regime in pulsed-pressure chemical vapor deposition. Chem Eng Sci 2007;62:6121–8.
[9] Siriwongrungson V. Characterisation of step coverage by pulsed-pressure metalorganic chemical vapour deposition: titanium dioxide thin films on 3-D micro- and nano-scale structures. Christchurch: University of Canterbury; 2010.
[10] Cave HM. Development of modelling techniques for pulsed pressure chemical vapour deposition (PP–CVD). Christchurch: University of Canterbury; 2008.
[11] Bird GA. Molecular gas dynamics and the direct simulation of gas flows. Oxford: Clarendon Press; 1994.
[12] Zwillinger D. CRC standard mathematical tables and formulae. 31st ed. Boca Raton, FL: CRC Press; 2003.
[13] Zhang H, Zhuang F. NND schemes and their applications to numerical simulation of two- and three-dimensional flows. Adv Appl Mech 1991;29:193–256.
[14] Van Leer B. Towards the ultimate conservative difference scheme III. Upstream-centered finite-difference schemes for ideal compressible flow. J Comput Phys 1977;23:263–75.
[15] Roe PL. Characteristic-based schemes for the Euler equations. Ann Rev Fluid Mech 1986;18:337–65.
[16] Ponchaut NF, Hornung HG, Pullin DI, Mouton CA. On imploding cylindrical and spherical shock waves in a perfect gas. J Fluid Mech 2006;560:103–22.
[17] Rudinger G, Somers LM. Behaviour of small regions of different gases carried in accelerated gas flows. J Fluid Mech 1960;7:161–76.
[18] Haas J-F, Sturtevant B. Interaction of weak shock waves with cylindrical and spherical gas inhomogeneities. J Fluid Mech 1987;181:41–76.
[19] Picone JM, Boris JP. Vorticity generation by shock propagation through bubbles in a gas. J Fluid Mech 1988;189:23–51.
[20] Smith MR. The true direction equilibrium flux method and its application. Brisbane: The University of Queensland; 2008.
[21] Bagabir A, Drikakis D. Mach number effects on shock-bubble interaction. Shock Waves 2001;11:209–18.
[22] Emery AF. An evaluation of several differencing methods for inviscid fluid flow problems. J Comput Phys 1968;2:306–31.
[23] Woodward P, Colella P. The numerical simulation of two-dimensional fluid flow with strong shocks. J Comput Phys 1984;54:115–73.
[24] Keats WA, Lien FS. Two-dimensional anisotropic Cartesian mesh adaptation for the compressible Euler equations. Int J Numer Methods Fluids 2004;46:1099–125.
[25] Smith MR, Macrossan MN, Abdel-jawad MM. Effects of direction decoupling in flux calculation in finite volume solvers. J Comput Phys 2008;227:4142–61.
[26] Cave HM, Tseng K-C, Wu J-S, Jermy MC, Lian Y-Y, Krumdieck SP et al. Modelling unsteady processes with the direct simulation Monte Carlo technique. In: Peter Jacobs TM, Matthew Cleary, David Buttsworth, David Mee, Rose Clements, Richard Morgan and Charles Lemckert, editors. 16th Australasian fluid mechanics conference (AFMC). Gold Coast, Queensland, Australia: School of Engineering, The University of Queensland; 2007. p. 1026–32.
[27] Chang I-S, Chang C-L, Chang S-C. Unsteady Navier–Stokes rocket nozzle flows. In: 41st AIAA joint propulsion conference. Tucson, AZ2005. p. 2005–4353.
[28] Boyd ID, Chen G, Candler GV. Predicting failure of the continuum fluid equations in transitional hypersonic flows. Phys Fluids 1995;7:210–9.
[29] Titov EV, Levin DA. Extension of the DSMC method to high pressure flows. Int J Comput Fluid Dyn 2007;21:351–68.
[30] Jermy MC, Lim C-W, Cave HM. Validity and inherent viscosity of the Quiet Direct Simulation method. In: 27th Intl symposium on rarefied gas dynamics 2010. Asilomar, California; 2010.